Manuscript

Click here to access/download;Manuscript;Igonin_etal.SourceSpectra.10_Cl

Spectral characteristics of hydraulic-fracturing induced seismicity can distinguish between activation of faults and fractures

Nadine Igonin[1*], Daniel T. Trugman[2], Keyla Gonzalez[3], and David W. Eaton[4]

1. Bureau of Economic Geology, Jackson School of Geoscience, University of Texas at Austin, Austin, Texas, U.S.A.

2. Nevada Seismological Laboratory, University of Nevada, Reno, U.S.A.

3. Tomlinson Geophysical Services Inc. (TGS), Houston, Texas, U.S.A.

4. Department of Geoscience, University of Calgary, Calgary, Alberta, Canada.

* Corresponding Author. Email: nadine.igonin@beg.utexas.edu

ABSTRACT

Analysis of earthquake spectra can aid in understanding source characteristics like stress drop and rupture complexity. There is growing interest in probing the similarities and differences of fault rupture for natural and human-induced seismic events. Here we analyze waveform data from a shallow, buried geophone array that recorded seismicity during a hydraulic fracturing operation near Fox Creek, Alberta. Starting from a quality-controlled catalog of 4,000 events between magnitude 0 and 3.2, we estimate source spectral corner frequencies using methods that account for the band-limited nature of the sensor response. The stress-drop values are found to be approximately self-similar, but with a slight magnitude dependence in which larger events have higher stress drop (~10 MPa). Careful analysis of the relative corner frequencies shows that individual fault and fracture segments experienced systematic variations in relative corner frequency over time, indicating a possible change in the stress state. Clustering analysis of source spectra based on the relative proportion of high and low frequency content relative to the Brune model further shows that event complexity evolves over time. Additionally, the faults produce earthquakes with systematically larger stress drop values than the fractures. Combined, these results indicate that the features activated by hydraulic fracturing experience observable changes in source behavior over time and exhibit different properties depending on the orientation, scale and fabric of the structural feature on which they occur on.

1. INTRODUCTION

Induced seismicity initiated by hydraulic fracturing has been observed worldwide (Atkinson et al., 2020; Schultz et al., 2020) and has been associated with events up to magnitude 5.7 (Lei et al., 2020). In general, hydraulic fracturing can trigger moderate magnitude seismicity by interaction with pre-existing faults (e.g., Chang and Segall, 2016; Wang et al., 2020). As such, there is much that can be learned from careful analysis of injection induced seismicity that is relevant to natural seismicity (Ellsworth, 2013).

Source spectral analysis has been used for decades to determine the corner frequency, stress drop, directivity and source complexity of earthquakes (Aki, 1972). These parameters are useful for understanding the rupture style and relative earthquake scaling, such as low vs. high stress drop. There has been considerable debate about whether stress-drop values from induced earthquakes are comparable to those from natural earthquakes. Many studies show evidence that stress drop from injection induced earthquakes is lower than their tectonic counterparts (Abercrombie and Leary, 1993; Boyd et al., 2017; Chen and Shearer, 2013, 2011; Fehler and Phillips, 1991; Goertz-Allmann et al., 2011; Hough, 2015, 2014; Reiter et al., 2012; Sumy et al., 2017; Yu et al., 2020); conversely, many studies show that stress-drop values of induced earthquakes are consistent with natural earthquakes at the same depth (Clerc et al., 2016; Holmgren et al., 2019; Huang et al., 2017; Spottiswoode and McGarr, 1975; Tomic et al., 2009; Zhang et al., 2019). Therefore, analysis of the corner frequency and stress drop of earthquakes from injection induced seismicity, especially at lower magnitudes, is of interest to further understand these observations.

There are many different techniques for analyzing spectra, including spectral fitting and empirical Green's functions (Abercrombie, 2021). Spectral fitting involves fitting a model of the displacement spectrum *S*(*f*) to the observed data,

$$S(f) = \frac{\Omega_0 e^{\frac{-\pi f t_0}{Q}} e^{-\pi\kappa f}}{\left[1+\left(\frac{f}{f_c}\right)^{\gamma n}\right]^{\frac{1}{\gamma}}} \quad , \qquad [1]$$

where Ω_0 is the low-frequency spectral amplitude, t_0 is the travel time to the sensor from the origin, Q is the quality factor that describes path attenuation, f_c is the corner frequency, κ is the site attenuation parameter (Anderson and Hough, 1984), γ is a constant controlling the spectral shape, and n controls the rate of high-frequency falloff (Abercrombie, 1995). The shape constant γ is assigned a value of 1 for the Brune model and 2 for the Boatwright model, and the falloff is typically set to 2 (Boatwright, 1980; Brune, 1970). There is a tradeoff between Q and κ, both of which relate to the attenuation of waveforms at different frequencies. Obtaining an independent estimate of Q and κ is desirable, but often not possible in practice (e.g. Atkinson and Silva, 1997; Hassani et al., 2011). In the following sections, we will describe the methods we used to try to determine an estimate for these parameters. Then, Equation [1] is used to solve for the corner frequency, which can be further related to other characteristics of the source, such as the stress drop.

Empirical Green's functions (EGFs) can also be used to remove path and site effects (e.g. Baltay et al., 2011; Mori and Frankel, 1990). This approach uses small events that occur in close proximity to a larger target event as a reference event, to remove the path/site effects that all the events have in common. Although the EGF method was developed using larger earthquakes (Hough, 1997), it has also been shown to be valuable when applied to small magnitude ($M < 2$) datasets (e.g. Imanishi and Ellsworth, 2006). Later in this paper, we use this approach to help constrain the potential Q values for our dataset.

The dataset used in this study is from a dense local geophone array near Fox Creek, Alberta, a region that has been associated with hydraulic-fracturing induced seismicity with magnitudes up to 4.2 (Schultz et al., 2020). As part of the monitoring strategy, a local, shallow-buried 10 Hz geophone array was used to determine precise locations and provide detailed insight into the induced seismicity (Eaton et al., 2018). Although this provides high-resolution epicentral locations, the use of geophones introduces a bandwidth limitation. The use of this type of sensor for estimation of source parameters has been successful, but often carries a larger uncertainty than broadband seismometer-based datasets (Klinger and Werner, 2021). For this reason, in this paper we employ several different strategies to constrain and account for the precise ranges of frequencies within which spectral analysis can be reliably carried out. We also impose strict quality-control criteria based on uncertainty calculations.

The goal of obtaining a catalog of corner frequencies and stress drops is to analyze if there are any statistically significant differences between the faults and fracture networks that were activated. In this paper, a fault is defined as a discontinuous surface across which there is a net shear displacement (Childs et al., 2009; Davatzes and Aydin, 2003; Peacock et al., 2016), while a fracture is a discontinuous surface across which there has been separation (Pollard and Aydin, 1988). Unlike fractures, faults generally contain core zones with gouge material formed by repeated failure. As such, fractures and faults have different geomechanical characteristics, which may be manifested in the stress drop or source complexity (e.g. Candela et al., 2011). In the absence of drillcores or image-log data, distinguishing between faults and fractures must rely on indirect measurements from earthquakes, such as b-values; seismicity due to fault activation tends to have b-values close to 1, while microseismicity associated with fractures is characterized by b-values closer to 2 (e.g. Eaton and Maghsoudi, 2015; Igonin et al., 2018).

In this paper, we start by introducing the Tony Creek dual Microseismic Experiment (ToC2ME) dataset, a high-resolution passive seismic dataset that recorded small earthquakes induced during hydraulic-fracturing operations. We use the highest quality events from this dataset for source-spectral analysis, estimation of Q, empirical Green's functions and spectral fitting. After obtaining robust estimates for the corner frequencies of each event, we calculate the static stress drop and the residual source spectra (i.e. the difference between the observed and model-predicted spectra), which are later used for clustering analysis and evaluation of source complexity (Uchide and Imanishi, 2016). Through this, we demonstrate that there are differences between the distribution of corner frequencies, stress drop and frequency content of event populations depending on whether they originate from faults or fractures.

2. Data and Results

2.1. ToC2ME dataset

The Tony Creek Dual Microseismic Experiment (ToC2ME) is a passive seismic dataset acquired west of Fox Creek, Alberta, Canada that recorded seismicity near a 4-well hydraulic fracturing pad in late 2016 (Eaton et al., 2018). This dataset has been extensively studied and interpreted (Igonin et al., 2021, 2018; Zhang et al., 2019) and contains at least 18,040 events that occurred during hydraulic-fracturing operations (Figure 1a). The station distribution (blue triangles, Figure 1b) makes it suitable for source-spectral analysis due to the azimuthal coverage and close proximity to the seismicity, which occurred at an average depth of 3.5 km below the surface. Three-component 10 Hz geophones were deployed in 69 shallow borehole arrays 27 m deep, which is below the weathering layer in this region. For this reason, geophone waveforms are relatively unaffected by near-surface attenuation and are thus characterized by relatively high signal-to-noise ratios (SNR), even for small earthquakes. Out of 18,040 events, 4,083 events have a signal to noise ratio (SNR) of over 5 on all stations, calculated by dividing the root-mean-square of the windowed signal by the root-mean-square of windowed noise before the signal. P- and S-wave picks are available at most of the stations for this high SNR event subset used in this paper. There were also six broadband seismometer stations deployed for the program, but they were not used for this analysis due to the higher noise conditions at the surface (Paes, 2020; Zhang et al., 2019).

There are three primary kinds of seismicity observed for this dataset (Figure 1a), as detailed by Igonin et al. (2021):

1. Fault activation (NS1-3): seismicity on linear structures, clusters having a *b*-value of ~1. NS1 and NS2 are on near-vertical strike-slip faults and contain the largest events of the sequence. NS3 is on a regional N/S trending fault and consists largely of normal faulting mechanisms, although the seismicity follows a NE/SW trend that straddles the primary fault structure. All of these event hypocenters are located above the injection zone.
2. Fracture network activation (NESW): A broad clustering of NE/SW parallel features that have *b*-values close to 2, are above the injection zone, and have strike-slip focal mechanisms consistent with the feature orientation.
3. Operational microseismicity: Within the injection depth and with a timing that matches the injection schedule. These events are within 100-200 m of the injection well and represent a minority of events within the 18,040 event catalog.

The events studied in this paper belong to either type 1 or 2; all of the operational seismicity had SNR values that were too small for source analysis. A primary aim of this paper is to determine if there are systematic, statistically-significant differences in the source characteristics of the events depending on whether they occur on faults or fractures.

2.2. Instrument response correction and displacement spectra calculation

The first step in the analysis was to perform an instrument-response correction to the data acquired using 10 Hz geophones (OYO GSX type) with a sampling rate of 0.002 seconds. Due to the stronger attenuation of the S-waves in the shallow subsurface, we focus our analysis on the P-waves only (Eaton et al., 2018). The data were first de-trended and tapered using a maximum percentage of 0.01. The instrument response correction was carried out on the vertical-component of the data windowed around the P-wave pick (10 samples before the pick and 160 samples after the pick). The ObsPy package (Beyreuther et al., 2010) was used for removing the instrument response, with a pre-filter of [0.5, 2.0, 200, 250].

For the 4076 events (median of 58 stations per event) we estimate the displacement spectra at each station using a multi-taper algorithm (Prieto, 2022) to calculate the power-spectral density. We used a time bandwidth product of 3.5 and set the number of tapers to 5 (e.g. Viegas et al., 2010). Then, we convert to displacement, and resample all the spectra to equal log-spacing.

2.3. Corner frequency and residual source spectra

2.3.1. *Q* estimation and spectral fitting

Two different approaches were used to constrain the P-wave attenuation (Q_P) value for this dataset. The first method uses EGF analysis, which resulted in a Q_P estimate of 50-80 (see Supplementary Material for details and results). There are limitations with these results, such as the small sample size (only 6 usable corner frequencies from the EGF method), and the narrow range of frequencies that could be used for the spectral fitting so there is significant uncertainty with this estimate. This first-order estimate is consistent with findings for Q_P close to the study region, which range from 25 to 75 (Bosman et al., 2015; Calixto and van der Baan, 2015).

To narrow down the range, we then used an iterative fitting of the source spectra (using Equation [1]) with different Q_P and κ values. By comparing the error for the total catalog for different trial values, we can more precisely determine an appropriate Q_P/κ combination for this dataset. Figure 2a shows the individual displacement spectra and median displacement spectra for one event across the 69 stations. The vertical dashed lines show the upper and lower limits for the fit, which are based on the signal to noise ratios in the frequency domain for each event. The lower frequency limit was fixed to the value where the lower frequency band range SNR first exceeded 2 (20-30 Hz for the smallest events) and defaulted as a minimum of 10 Hz for the larger events, due to the limited geophone sensitivity at low frequencies. The upper frequency limit also corresponded to the highest frequency value where the SNR remained above the threshold value of 2. This value is lower than many studies, which typically suggest using a SNR of 3-10 (Klinger and Werner, 2021; Oth et al., 2011; Shearer and Abercrombie, 2021; Trugman et al., 2017), but given the bandwidth limitations, we opted for a lower bound to allow for a broader frequency range that was still suitable for our spectral fitting approach. Since the true low-frequency plateau (at 0 Hz) cannot be determined from the raw data, we estimate Ω_0 by assuming an initial stress drop of 1 MPa to calculate the theoretical corner frequency for each given event given an estimate of the seismic moment (using Equation 1). Then, we use the observed amplitude at 10 Hz, the trial f_c, and theoretical f_c to get the theoretical low-frequency plateau at 0 Hz (see Supplementary Material). The L_2 norm is then used to minimize the misfit between the observed and modelled data. The best-fit model is shown in Figure 2b; in the illustrated case, it resulted in a corner frequency of 17 Hz for the M 0.65 event.

We then used the best-fit model to obtain residual spectra, defined as the difference between the observed spectra and the best-fit model. This gives a measure of the *relative* proportion of frequency that is either above or below the model value. We also use the residual to calculate the median absolute error for each event. The error was calculated for each event using Q values of ranging between 50 and 140, κ = 0-0.011, using both the Brune (n=1) and Boatwright (n=2) models. Comparisons of the medians of the histograms of errors for each of the versions of the catalogs showed that, for both the Brune and Boatwright models, Q_P = 80 and $\kappa = 0.007$ provided the best fit (see Supplementary Material for a comparison of the histograms). Additionally, the Boatwright models consistently had lower error than the Brune models. Therefore, for the remainder of the paper, we use the Boatwright model for the fit, a Q_P value of 80 and $\kappa = 0.007$. This is in close correspondence with Rodríguez-Pradilla and Eaton (2019), who found a Q_P of 60 for this same dataset.

2.3.2. Bootstrap uncertainty analysis and corner frequency

With the parameters for fitting Equation [1] to the data sufficiently constrained, we calculated uncertainties in the corner frequencies for the events using bootstrapping. During each bootstrap iteration, we re-sampled the 69 station spectra with replacement, keeping the total number of spectra to 69 each time. Then, we calculated the median of the station spectra in each resampled instance and carried out the spectral fitting on the median, solving for the corner frequency (Figure 2b). This was repeated 500 times and the median corner frequency from the 500 iterations was taken as the corner frequency for that event. An example histogram of the distribution of corner frequencies for a well-constrained event and a poorly-constrained event can be found in the Supplementary Material (Figure S9). The standard deviation of f_c obtained from bootstrapping for each event ranged from 5-80 Hz (Supplementary Material). In the following section we will impose a cut-off of standard deviation of 10 Hz for the uncertainty. We acknowledge that this is a large range, further illustrating the challenges of working with band-limited data.

2.4. Stress drop

To estimate stress drop, we used the expression

$$\Delta\sigma = \frac{7}{16} M_0 \left(\frac{f_c}{k v_s}\right)^3 \quad , \qquad [2]$$

where k is a numerical constant, and v_s is the S-wave velocity in the source region (Eshelby, 1957). Based on the numerical results of Kaneko and Shearer (2014), we set $k = 0.38$, appropriate for P-wave spectra. From nearby well log data, we set v_s to 2100 m/s. The corner frequency is known from the bootstrap analysis.

Although estimates of M_0 are available from Igonin et al., 2018, for consistency, we re-calculated the M_0 and M_W for this dataset using a similar approach to the corner frequency, using the median of the spectral amplitudes from 5 to 20 Hz as a reference point for the low-frequency plateau for this dataset. The updated magnitudes match very closely with the original magnitudes, but there is some minor deviation for a small subset of events at M_W < 0.5 (Supplementary Material). Uncertainties for M_0 were calculated using a bootstrap approach in the same way as for the corner frequency.

Figure 3 shows a crossplot of the corner frequency with the moment. The events are colored based on standard deviation, and whether the inverted corner frequency is within the SNR > 2 range for each individual event. The uncertainty criterion preferentially eliminates events with higher corner frequencies, which is expected due to the low signal to noise ratios for most events above 80 Hz.

In order to quantify apparent departure from self-similarity, we fit a linear equation to the data binned at increments of 0.2 in the $\log_{10}(M_0)$ domain (Kanamori, 2004; Trugman et al., 2017; Walter et al., 2006). The linear equation is

$$\log_{10} f_c = \psi_0 + \psi_1 \log_{10} M_0 \quad . \qquad [3]$$

Based on the implied trend-line, we then calculate the normalized, magnitude-corrected corner frequency, which is given by:

$$Z_{fc} = \frac{\log_{10} f_c - E[\log_{10} f_c | M_0]}{STD\{\log_{10} f_c - E[\log_{10} f_c | M_0]\}} \quad , \qquad [4]$$

where E[] refers to the expected corner frequency based on an input M_0 and the constants from Equation [3]. Positive values indicate corner frequencies that are larger than the line of best fit, while negative values correspond to smaller-than-expected corner frequencies. This re-parameterization of the dataset allows us to distinguish events that are enriched or depleted in high-frequency energy compared to typical events of the same size. According to the parameterization in Equation (3), a ψ_1 value of -0.333 corresponds to a self-similar relationship; smaller negative ψ_1 values indicate an increase in the stress drop with magnitude, while larger negative ψ_1 values correspond to a decrease in stress drop with magnitude. For this dataset, ψ_1 has a best-fit value of -0.198. It should be noted that for the magnitude range of 1.2 to 2.5, a linear fit yields a ψ_1 value of -0.28, closer to self-similarity. Due to the band-limited nature of the geophones, it is possible that apparent breakdown in self-similarity reflects insufficient SNR at higher frequencies, which leads to an apparent decrease in the event corner frequency. The expected corner frequencies for the events of magnitude 1.2 to 2.5 are on the order of 10-30 Hz, which is well-resolved given the signal to noise relationships discussed previously.

Analysis of normalized corner frequency reveals coherent spatial and temporal trends. In Figures 4-5, we use a colorscale where blue denotes positive normalized corner frequencies (enriched in high-frequency energy) and red denotes events with negative normalized corner frequencies (depleted in high-frequency energy). Each of the clusters (as labeled in Figure 1) exhibit different behavior over time. NS1, the largest N/S trending feature, begins with consistently lower normalized corner frequencies, but then towards the end of the acquisition period shifts to consistently higher normalized corner frequencies (Figure 4a,c). NS3, which resides on a regional N/S trending fault, has an opposite trend to NS1, in that the sequence begins with higher normalized f_c and then shifts to lower overall normalized f_c values over time (Figure 4b,d). An animation of the normalized corner frequency over time relative to the operations schedule is included in the supplementary material.

Figure 4 also shows the timing of the hydraulic fracturing stages relative to the event progression. The event locations closely follow the nearest hydraulic fracturing stages, and injection can be clearly attributed as the cause of activation (see also Igonin et al., 2021). Well C was hydraulically fractured first and used an atypical completion procedure, with many closely-spaced small-volume stages (1 perforation shot per stage). During the completion of well C, the NESW cluster was activated, as well as the southern half of NS1. After all of the stages of well C were done, operations began on wells A, B, and D concurrently. These wells were hydraulically fractured using a zipper approach with the plug-and-perf method (Eaton, 2018), with 4 perforation shots per stage. Wells A, B and D featured larger volumes and larger stage spacing than well C. Well A, which is the closest well to NS3, is interpreted to be responsible for the activation of that fault feature. The data collection using the shallow buried array was completed prior to the end of the hydraulic fracturing programs, so only half of the stages of wells A, B and D were recorded.

The NE/SW trending features are shown together over time in Figure 5. Collectively, there is an overall negative normalized corner frequency across the entire sequence, with two exceptions. At the onset, there is a reversal of normalized f_c from negative to positive (dashed region in Figure 5). There is also an increase in normalized f_c toward the end of the data-collection period, and this corresponds to a magnitude 3 event occurring at the intersection of one of the parallel NE/SW trending features and the northern part of NS1.

In terms of the injection timing, the NESW clusters were first activated during the hydraulic fracturing of well C. The largest central portion of the NESW clusters was activated twice; the second time being during the closest stages of well B.

From the combined behaviour of the events on faults and fractures, we postulate that the events on the faults are more likely to have higher normalized corner frequency, whereas fractures are more likely to have lower normalized corner frequency. Both features exhibit reversals from one mode to the other. In the Discussion section, we explore these observations further.

2.5. Spectral clustering analysis

To analyze the corner frequency and how the proportion of high- and low-frequency content varies for each event, we calculate residual spectra using the best-fit Boatwright model at the inverted corner frequency, $S\,(f\,|\,f_c)$, and the observed spectra $S^*(f)$:

$$R_S(f) = \log_{10} S(f|f_c) - \log_{10} S^*(f) \quad . \qquad [5]$$

The residual spectra provides a measure of the relative proportions of frequency above/below the best-fit model (Uchide and Imanishi, 2016). For example, some events may have higher proportions of higher frequency energy, while others may have decreases in frequency content in other frequency bands. These relative proportions within different frequency bands reflect event complexity; departure from the Boatwright best-fit model is inferred to represent complex rupture. By clustering the residual spectra into groups, we can determine if there are any consistent trends that correlate with either spatial features (fractures vs. faults) or the timing of the earthquakes.

For this purpose we use a spectral clustering algorithm (e.g. von Luxburg, 2007) implemented in scikit-learn, a Python package (Pedregosa et al., 2011). We window the data in the range [20,60 Hz], because the majority of events have SNR > 2 within that range, whereas only the larger events have energy outside that band. As a quality-control step, we use only the residual spectra for events where the standard deviation of the corner frequency was less than 20 Hz, resulting in a subset with 3078 events. The spectral clustering algorithm requires a few hyperparameters: the number of clusters, the affinity metric, and the number of neighbors. We set the number of clusters to 8 and use the cosine affinity with 10 neighbors. Figure 6 shows the normalized residual spectra, by cluster, within the frequency band that was used.

All of the clusters are negative or close to zero at less than 30 Hz, suggesting that the best-fit Boatwright model underestimates the lower frequencies (Figure 6). This corresponds to an observation of the geophone data having low-frequency noise that results in an increase in low-frequency content (as seen in Figure 2). Each of the clusters have a different prevalence of energy within the [30 60] Hz band, and some clusters show notches at specific frequencies. An interesting note is that most of the clusters are approximately the same size (on the order of 100s of events), with the exception of cluster 5, which only contains 5 events that have spectra that does not visually match any of the other clusters. Excluding this small cluster, we can classify three broad groups. First, clusters 1 and 2 are similar and have the largest deviations from the Boatwright model (dashed line at zero residual), Second, clusters 3 and 4 are similar to each other, but have smaller residual values than clusters 1 and 2. Third, clusters 5, 6 and 7 all display notches at 32, 44 and/or 52 Hz, but are the closest to having zero residual.

To study the significance of the clustering further, Figure 7 shows a time series of the clusters obtained from spectral clustering, with each subplot showing the proportion of each cluster in a) NS1, b) NS3, and c) NESW with the colors matching Figure 6. Both fault features (NS1 and NS3) are dominated by cluster 1 (yellow). Clusters 2, 3 and 4 (orange and greens) are also prevalent in both fault features. In contrast, the NESW clusters show more diversity in the spectral clusters, and clusters 5, 6 and 7 (purple, and blues) are more present. In the Discussion, we explore the potential significance of these differences.

Figure 7d shows a map view of the events colored by the clusters from the spectral clustering algorithm. Cluster 3 (light green) is present in all the features, which shows that the spectral clustering is not biased based on the source location. Likewise, cluster 2 (orange) is seen in both NS1 and NS3, though both of them are from opposite ends of the study area. Therefore, we believe that the data processing and careful selection of usable frequencies has removed biases associated with events coming from the same location. Similarly, there is no magnitude dependence with the clusters (see Supplementary Material), since they occur equally for all magnitudes.

3. DISCUSSION

In this section we start by discussing the limitations of the results and sources of uncertainty and bias in the data. Then, we split the normalized corner frequency values depending on which feature they originate (fault vs. fracture), to show there are statistically significant differences. Finally, we discuss the results of the spectral clustering analysis in more detail and integrate those results with the observations from the corner-frequency distributions to make inferences about seismicity along faults and fractures.

3.1. Sources of uncertainty

The bandlimited nature of the geophone data introduces difficulties in determining accurate corner frequencies and stress drops. For example, Ide and Beroza (2001) demonstrated that bandlimited data can cause apparent deviation of self-similarity of stress drop with magnitude due to an underestimation of the radiated energy. Likewise, there are challenges in determining the Q and κ values independently and accurately (Ktenidou et al., 2014). Some studies have shown that is it possible to get corner frequencies and stress drop values from geophone data that is consistent with that observed with broadband seismometer data (e.g. Glasgow et al., 2018; Goertz-Allmann et al., 2011; Klinger and Werner, 2021; Viegas et al., 2012), though in all cases similar challenges were faced with the data processing.

Although we found a breakdown in scaling for the stress drops in this study (Figure 3), the robustness of this observation is limited by the narrow range of frequencies with good SNR (e.g., Ruhl et al., 2017). However, there are several plausible physical mechanisms that could cause deviations from self-similarity, and number of studies have reported such trends (Bindi et al., 2020; Oth et al., 2011; Pacor et al., 2016; Trugman, 2020; Trugman et al., 2017; Trugman and Shearer, 2018, 2017; Wang et al., 2019). A systematic change in rupture velocity, fault geometry or rupture aspect ratio could perturb the measured corner frequency (e.g. Kaneko and Shearer, 2015; McGuire and Kaneko, 2018) in a manner that could be interpreted as a magnitude-dependent stress drop. Similarly, larger earthquakes are preferentially more likely to activate frictional weakening mechanisms that could lead to higher stress drops (e.g., Tullis, 2015). In the case of induced seismicity, it also is possible that small and large earthquakes are fundamentally different, with smaller events usually associated with anthropogenic stressing and stress release, and larger ones triggered by, or relieving, anthropogenic stresses (Ellsworth et al., 2019). In this case, there was a combination of fault and fracture related events, which may further explain the difference in scaling if there are two superimposed distributions (e.g., Yu et al., 2020). The band-limited nature of our dataset prevents us from making any strong claim in these regards.

Another source of uncertainty is the fixed high-frequency falloff rate, represented by the parameter n (Shearer et al., 2019; Trugman, 2022, 2020; Trugman and Shearer, 2017; Yin et al., 2018). Broadly speaking, a falloff rate defined by $n = 2$ is consistent with observations for most earthquakes (Hough, 2001), but minor deviations have been observed and can be attributed to increasing the uncertainty in the inverted corner frequency and stress drop (Walter et al., 2017). Especially in the case of geophone data, constraining n is an added challenge (Klinger and Werner, 2021; Yenier et al., 2016).

3.2. Stress drop distribution by feature type

One observation made by analysing the spatial distribution of the normalized corner frequency is that the events located on faults tend to have higher normalized f_c than those on fractures. To analyze this further, Figure 8 shows a histogram comparing normalized f_c from faults (NS1-3) vs. fractures (NESW). The median of the normalized f_c of the faults is 0.21, and the median of the normalized f_c of the fractures is -0.25. However, it should be noted that most of the largest events within the dataset ($M_W > 2$) have low normalized f_c values (Figure 3).

This difference in distributions suggests that earthquakes on faults release more high-frequency energy than comparably sized events on fractures. Both populations of events occurred at the same depths (Poulin et al., 2019), so the differences in the normalized corner frequency are not related to differences in the depth. These differences may reflect geomechanical differences between faults and fractures; that is the properties of the faults allow them to sustain higher stress-drop events than fracture networks. Laboratory studies show a link between fault heterogeneity and stress drop, with larger stress drops for smooth, homogeneous faults (Goebel et al., 2013, 2015). Fractures in this context may be thought of as immature fault surfaces, which lack the strength and smoothness of more mature fault surfaces; the increased relative roughness of the fractures may be what prevents them from experiencing higher relative stress drops. Furthermore, it is likely that the faults and fractures have different frictional stability, as brittle fault materials are more likely to be associated with larger stress drops (Gu and Wong, 1991; He et al., 2003; Rubin and Ampuero, 2005). Both the faults and fractures are located within the Ireton Formation, which is a shale unit with low organic content (Knapp et al., 2017). This formation itself would be classified as more ductile than brittle, but there is documented lateral heterogeneity based on seismic data from the study region (Weir et al., 2018). The fault rheology is expected to differ from the host formation due to the presence of fault gouge material. The mineralogical content of the fault gouge in this region is likely a combination of Ireton-derived material, and material brought by fluid upwelling from the Precambrian basement (Galloway et al., 2018).

The intraplate setting of this study area also likely plays a role; laboratory experiments show that longer interseismic periods lead to an increase in asperity strength and stress drop on a fault (Beeler et al., 2001). That is, due to the longer healing time, the faults in the Fox Creek region have well-developed asperities and non-negligible cohesion, which may then allow for the build-up of larger stresses on the fault. Similar observations have been made in Oklahoma when comparing slip on a fault that was activated due to fluid injection and slip on faults in tectonically active regions (Pennington et al., 2022). In any case, in the absence of drillcore data from faults and fractures, neither of these possibilities can be conclusively tested.

3.3. Clustering analysis

Analysis of the residual spectra into clusters using the spectral clustering algorithm shows that there are distinct families of spectra for the ToC2ME dataset. These families show some preference for the host type of structure (Figure 7). The clusters that are the most prevalent on the fault features (clusters 1, 2 and 4) are the least prevalent on the fractures, with the exception of cluster 3 which is prevalent on both types of features. As evident in Figure 6, each of these clusters has a similar type of residual spectra - relatively smooth and positive in the 35-50 Hz range. In contrast, residual spectra associated with the events on the fractures (clusters 5, 6 and 7) are all closer to the best-fit model, and have peaks at 42 and/or 52 Hz. This leads us to the conclusion that there is a distinct difference between the source spectra of faults and fractures.

A physical interpretation of the spectral complexity is that it may be indicative of subevents (e.g., Wu et al., 2019; Ye et al., 2016). Subevents are caused by different portions of a fault surface experiencing displacement at different times, but close enough in time that they are nevertheless considered to be one earthquake. One cause of such behaviour is fault-surface heterogeneity, which has been observed for moderate-to-small earthquakes in the same magnitude range as those presented here (Abercrombie, 2014; Abercrombie et al., 2020; Chen et al., 2016; Ide, 2001; Ruhl et al., 2017; Uchida et al., 2015; Wang et al., 2014; Yamada, 2005). In this study, observations point to two types of rupture surfaces, with their own modes of heterogeneity, which then causes the residual spectra of the faults and fractures to be distinct. Another possible interpretation is that if rupture is actually continuous (no subevents), then complex spectra may arise from interference of stopping phases (Ben-Menahem, 1961; Madariaga, 1976). These stopping phases are present in cases of runaway rupture when the rupture area reaches a boundary (Wen et al., 2018). Given the geological limitations on the fault dimensions in this study area, and the two types of rupture surfaces, both subevents and runaway rupture in bounded strata may explain the spectral complexity.

Comparing the time series of the spectral clustering analysis (Figure 7) to the results of the normalized corner frequency over time (Figures 4 and 5) does not indicate any significant trends. Both the fault and fracture features experience reversals in the normalized corner frequency over time, but there is no clear link between those reversals and the prevalence of different clusters based on the spectral clustering. For example, NS1 starts with negative normalized f_c and has little spectral variability (cluster 1 is dominant); then NS1 ends with positive normalized f_c and there are many clusters active. Conversely, NS3 goes from positive to negative normalized f_c over time, and likewise contains several clusters. However, it should be noted that cluster 1 only became dominant around November 22, which corresponds to the reversal in normalized f_c. For the NESW events, many clusters are active throughout, and there is no distinct trend between the normalized f_c and cluster prevalence.

Another interesting observation is that events with similar spectra are more likely to occur at a time when there are many events of the same kind (e.g., the steepness of increase of the clusters in Figure 7c). This could be a reflection of a similar location or similar source properties (e.g., Trugman et al., 2020; Zhang et al., 2019). From an energy-balance perspective, it may be easier to sustain activity along the same feature than to divert energy into creating/activating new features.

Finally, we consider changes in the normalized corner frequency over time. One potential interpretation of the systematic transitions from positive to negative f_c (or vice versa) is that it is a reflection of the subsurface stress state. There is some evidence that there are higher stress drops in regions of higher background stress (Allmann and Shearer, 2009; Negishi et al., 2002; Pennington et al., 2021). For example, some studies have noted an increase in stress drop with depth, and one potential explanation for this is that the stresses are higher at depth (Goebel et al., 2015; Hardebeck and Aron, 2009; Hardebeck and Hauksson, 1997; Jones and Helmberger, 1996; Oth et al., 2010; Pacor et al., 2016; Shearer et al., 2006; Trugman et al., 2017; Venkataraman and Kanamori, 2004). Other studies have found temporal changes in stress drop as well, and attribute the changes to lateral or depth variability in the fault strength (Abercrombie, 2014; Oth and Kaiser, 2014; Sumy et al., 2017).

In this study, event magnitudes tend to be larger during periods when the normalized f_c is positive (such as during the M_W 3 events on NS1), and smaller when the normalized f_c is negative (such as during NS3 after the reversal to negative normalized f_c). This invites speculation that the average normalized corner frequency be used to determine if there will be a continuation of larger magnitude events. At the end of the recording period, the only cluster with positive normalized f_c is NS1. The preceding pattern suggests that this cluster is more likely to host larger events after the recording period ended. Indeed, after the cessation of recording on the local array, the regional broadband network picked up multiple events > M_W 2 from the approximate location of NS1 (see Table 1 in the Supplementary Material). More detailed studies in different regions and tectonic settings are required to determine if these observations are generally representative.

Altogether, the observations in this paper suggest that there are statistically significant differences between the corner frequencies and stress drops on different structural units (faults, fractures), likely reflecting their respective orientation, scale and fabric. These observations can be applied to natural fault systems where there is interaction with fractures, or other datasets with injection induced seismicity and pre-existing fracture networks. A temporal change in normalized f_c of induced seismicity, if shown to be indicative of the subsurface stress state as suggested by our data, represents an intriguing prospect as an indicator of elevated risk.

4. CONCLUSION

After comprehensive analysis of source spectra from the ToC2ME induced seismicity dataset, we show that there are significant differences between event populations located on faults and fractures, with on-fault events having larger normalized corner frequency (and therefore stress drop) than off-fault events. The events on the faults also show temporal changes in normalized corner frequency that we interpret as indicative of an evolving subsurface stress state. During times of higher normalized corner frequency events there is a greater likelihood of larger-magnitude events, which may correspond to periods of elevated subsurface stress due to the nearby injection. On-fault events show more variability in the residual spectra, and a larger departure from the best-fit source model. We observe a mild departure from self-similarity over three orders of magnitude, which may represent changes in rupture velocity, fault geometry or rupture aspect ratio, although it may simply reflect a limitation of geophone data. Combined, these observations indicate that there are distinctions between the corner frequencies, stress drops, and frequency content of earthquakes on faults and fractures.

Data and Resources

Continuous raw data (geophone and broadband recordings, network code 5B with start date: 2016-10-25 and end date: 2016-12-01) are available through the IRIS Data Center. The event catalogs used in this study are available at the ToC2ME GitHub website (https://github.com/ToC2ME, last accessed January 2023). Additional information about the ToC2ME dataset is also available at www.toc2me.com (last accessed January 2023). All of the figures were made using Matlab Software, which is available at www.mathworks.com/products/matlab (last accessed September 2022). The supplementary material contains further details on the workflow, empirical Green's functions analysis, error distributions by Q and κ value, additional information about bootstrapping, the re-calculated magnitudes, an animation of the normalized corner frequency over time, and additional plots of the spectral clustering results.

Declaration of Competing Interests

The authors acknowledge that there are no conflicts of interest recorded.

Acknowledgements

The authors are grateful to two anonymous companies for providing access for acquisition of the data. This research was supported in part by funding from SCEC Award 21017, NSF Award EAR-2146687, the Texas Seismological Network and Seismology Research Program of the Bureau of Economic Geology at the University of Texas, the Department of Geoscience at the University of Texas at Austin, and NSERC grant IRCPJ/485692-2014. We thank the sponsors of the Microseismic Industry Consortium for their financial support of this study.

References

Abercrombie, R., Leary, P., 1993. Source parameters of small earthquakes recorded at 2.5 km depth, Cajon Pass, southern California: Implications for earthquake scaling. Geophysical Research Letters 20, 4.

Abercrombie, R.E., 2021. Resolution and uncertainties in estimates of earthquake stress drop and energy release. Phil. Trans. R. Soc. A. 379, 20200131. https://doi.org/10.1098/rsta.2020.0131

Abercrombie, R.E., 2014. Stress drops of repeating earthquakes on the San Andreas Fault at Parkfield. Geophys. Res. Lett. 41, 8784–8791. https://doi.org/10.1002/2014GL062079

Abercrombie, R.E., 1995. Earthquake source scaling relationships from −1 to 5 M_L using seismograms recorded at 2.5-km depth. J. Geophys. Res. 100, 24015–24036. https://doi.org/10.1029/95JB02397

Abercrombie, R.E., Chen, X., Zhang, J., 2020. Repeating Earthquakes With Remarkably Repeatable Ruptures on the San Andreas Fault at Parkfield. Geophys. Res. Lett. 47. https://doi.org/10.1029/2020GL089820

Aki, K., 1972. Scaling Law of Earthquake Source Time-Function. Geophysical Journal International 31, 3–25. https://doi.org/10.1111/j.1365-246X.1972.tb02356.x

Allmann, B.P., Shearer, P.M., 2009. Global variations of stress drop for moderate to large earthquakes. J. Geophys. Res. 114. https://doi.org/10.1029/2008JB005821

Anderson, J., Hough, S.E., 1984. A model for the shape of the fourier amplitude spectrum of acceleration at high frequencies. Bulletin of the Seismological Society of America 74. https://doi.org/10.1785/BSSA0740051969

Atkinson, G., Silva, W., 1997. An empirical study of earthquake source spectra for California earthquakes. Bulletin of the Seismological Society of America 87, 97–113. https://doi.org/10.1785/BSSA0870010097

Atkinson, G.M., Eaton, D.W., Igonin, N., 2020. Developments in understanding seismicity triggered by hydraulic fracturing. Nat Rev Earth Environ 1, 264–277. https://doi.org/10.1038/s43017-020-0049-7

Baltay, A., Ide, S., Prieto, G., Beroza, G., 2011. Variability in earthquake stress drop and apparent stress. Geophys. Res. Lett. 38, n/a-n/a. https://doi.org/10.1029/2011GL046698

Beeler, N.M., Hickman, S.H., Wong, T. -f., 2001. Earthquake stress drop and laboratory-inferred interseismic strength recovery. J. Geophys. Res. 106, 30701–30713. https://doi.org/10.1029/2000JB900242

Ben-Menahem, A., 1961. Radiation of seismic surface-waves from finite moving sources. Bulletin of the Seismological Society of America 51, 401–435. https://doi.org/10.1785/BSSA0510030401

Beyreuther, M., Barsch, R., Krischer, L., Megies, T., Behr, Y., Wassermann, J., 2010. ObsPy: A Python Toolbox for Seismology. Seismological Research Letters 81, 530–533. https://doi.org/10.1785/gssrl.81.3.530

Bindi, D., Spallarossa, D., Picozzi, M., Morasca, P., 2020. Reliability of Source Parameters for Small Events in Central Italy: Insights from Spectral Decomposition Analysis Applied to Both Synthetic and Real Data. Bulletin of the Seismological Society of America 110, 3139–3157. https://doi.org/10.1785/0120200126

Boatwright, J., 1980. A spectral theory for circular seismic sources; simple estimates of source dimension, dynamic stress drop, and radiated seismic energy. Bulletin of the Seismological Society of America 70, 1–27. https://doi.org/10.1785/BSSA0700010001

Bosman, K., Preiksaitis, M., Baig, A., Urbancic, T., 2015. From Microseismic to Induced Seismicity: Monitoring the Full Band of Reservoir Seismicity, in: SEG Technical Program Expanded Abstracts 2015. Presented at the SEG Technical Program Expanded Abstracts 2015, Society of Exploration Geophysicists, New Orleans, Louisiana, pp. 4843–4847. https://doi.org/10.1190/segam2015-5931654.1

Boyd, O.S., McNamara, D.E., Hartzell, S., Choy, G., 2017. Influence of Lithostatic Stress on Earthquake Stress Drops in North America. Bulletin of the Seismological Society of America 107, 856–868. https://doi.org/10.1785/0120160219

Brune, J.N., 1970. Tectonic stress and the spectra of seismic shear waves from earthquakes. J. Geophys. Res. 75, 4997–5009. https://doi.org/10.1029/JB075i026p04997

Calixto, F.J., van der Baan, M., 2015. Three Dimensional Attenuation Tomography from Microseismicity, in: SEG Technical Program Expanded Abstracts 2015. Presented at the SEG Technical Program Expanded Abstracts 2015, Society of Exploration Geophysicists, New Orleans, Louisiana, pp. 2430–2434. https://doi.org/10.1190/segam2015-5829881.1

Candela, T., Renard, F., Bouchon, M., Schmittbuhl, J., Brodsky, E.E., 2011. Stress Drop during Earthquakes: Effect of Fault Roughness Scaling. Bulletin of the Seismological Society of America 101, 2369–2387. https://doi.org/10.1785/0120100298

Chang, K.W., Segall, P., 2016. Injection-induced seismicity on basement faults including poroelastic stressing: Induced seismicity on basement faults. J. Geophys. Res. Solid Earth 121, 2708–2726. https://doi.org/10.1002/2015JB012561

Chen, K.H., Chen, I., Kim, A., 2016. Can slip heterogeneity be linked to earthquake recurrence?: Geophys. Res. Lett. 43, 6916–6923. https://doi.org/10.1002/2016GL069516

Chen, X., Shearer, P.M., 2013. Correction to "Comprehensive analysis of earthquake source spectra and swarms in the Salton Trough, California." J. Geophys. Res. Solid Earth 118, 1193–1194. https://doi.org/10.1002/jgrb.50098

Chen, X., Shearer, P.M., 2011. Comprehensive analysis of earthquake source spectra and swarms in the Salton Trough, California. J. Geophys. Res. 116, B09309. https://doi.org/10.1029/2011JB008263

Childs, C., Manzocchi, T., Walsh, J.J., Bonson, C.G., Nicol, A., Schöpfer, M.P.J., 2009. A geometric model of fault zone and fault rock thickness variations. Journal of Structural Geology 31, 117–127. https://doi.org/10.1016/j.jsg.2008.08.009

Clerc, F., Harrington, R.M., Liu, Y., Gu, Y.J., 2016. Stress drop estimates and hypocenter relocations of induced seismicity near Crooked Lake, Alberta. Geophys. Res. Lett. 43, 6942–6951. https://doi.org/10.1002/2016GL069800

Davatzes, N.C., Aydin, A., 2003. Overprinting faulting mechanisms in high porosity sandstones of SE Utah. Journal of Structural Geology 25, 1795–1813. https://doi.org/10.1016/S0191-8141(03)00043-9

Eaton, D.W., Igonin, N., Poulin, A., Weir, R., Pellegrino, S., Rodriguez, G., 2018. Induced Seismicity Characterization during Hydraulic-Fracture Monitoring with a Shallow-Wellbore Geophone Array and Broadband Sensors. Seismological Research Letters 89, 11.

Eaton, D.W., Maghsoudi, S., 2015. 2b... or not 2b? Interpreting magnitude distributions from microseismic catalogs. First Break 33. https://doi.org/10.3997/1365-2397.33.10.83159

Ellsworth, W.L., 2013. Injection-Induced Earthquakes. Science 341, 1225942. https://doi.org/10.1126/science.1225942

Ellsworth, W.L., Giardini, D., Townend, J., Ge, S., Shimamoto, T., 2019. Triggering of the Pohang, Korea, Earthquake (Mw 5.5) by Enhanced Geothermal System Stimulation. Seismological Research Letters. https://doi.org/10.1785/0220190102
Eshelby, J., 1957. The determination of the elastic field of an ellipsoidal inclusion, and related problems. Proc. R. Soc. Lond. A 241, 376–396. https://doi.org/10.1098/rspa.1957.0133
Fehler, M., Phillips, W.S., 1991. Simultaneous inversion for *Q* and source parameters of microearthquakes accompanying hydraulic fracturing in granitic rock. Bulletin of the Seismological Society of America 81, 553–575. https://doi.org/10.1785/BSSA0810020553
Galloway, E., Hauck, T., Corlett, H., Pană, D., Schultz, R., 2018. Faults and associated karst collapse suggest conduits for fluid flow that influence hydraulic fracturing-induced seismicity. Proc. Natl. Acad. Sci. U.S.A. 115. https://doi.org/10.1073/pnas.1807549115
Glasgow, M.E., Schmandt, B., Hansen, S.M., 2018. Upper crustal low-frequency seismicity at Mount St. Helens detected with a dense geophone array. Journal of Volcanology and Geothermal Research 358, 329–341. https://doi.org/10.1016/j.jvolgeores.2018.06.006
Goebel, T.H., Schorlemmer, D., Becker, T.W., Dresen, G., Sammis, C.G., 2013. Acoustic emissions document stress changes over many seismic cycles in stick-slip experiments. Geophys. Res. Lett. 40, 2049–2054. https://doi.org/10.1002/grl.50507
Goebel, T.H.W., Sammis, C.G., Becker, T.W., Dresen, G., Schorlemmer, D., 2015. A Comparison of Seismicity Characteristics and Fault Structure Between Stick–Slip Experiments and Nature. Pure Appl. Geophys. 172, 2247–2264. https://doi.org/10.1007/s00024-013-0713-7
Goertz-Allmann, B.P., Goertz, A., Wiemer, S., 2011. Stress drop variations of induced earthquakes at the Basel geothermal site. Geophysical Research Letters 38, 5. https://doi.org/10.1029/2011GL047498
Gu, Y., Wong, T., 1991. Effects of loading velocity, stiffness, and inertia on the dynamics of a single degree of freedom Spring-Slider System. J. Geophys. Res. 96, 21677–21691. https://doi.org/10.1029/91JB02271
Hardebeck, J.L., Aron, A., 2009. Earthquake Stress Drops and Inferred Fault Strength on the Hayward Fault, East San Francisco Bay, California. Bulletin of the Seismological Society of America 99, 1801–1814. https://doi.org/10.1785/0120080242
Hardebeck, J.L., Hauksson, E., 1997. Static stress drop in the 1994 Northridge, California, aftershock sequence. Bulletin of the Seismological Society of America 87, 1495–1501. https://doi.org/10.1785/BSSA0870061495
Hassani, B., Zafarani, H., Farjoodi, J., Ansari, A., 2011. Estimation of site amplification, attenuation and source spectra of S-waves in the East-Central Iran. Soil Dynamics and Earthquake Engineering 31, 1397–1413. https://doi.org/10.1016/j.soildyn.2011.05.017
He, C., Wong, T., Beeler, N.M., 2003. Scaling of stress drop with recurrence interval and loading velocity for laboratory-derived fault strength relations. J. Geophys. Res. 108. https://doi.org/10.1029/2002JB001890
Holmgren, J.M., Atkinson, G.M., Ghofrani, H., 2019. Stress Drops and Directivity of Induced Earthquakes in the Western Canada Sedimentary Basin. Bulletin of the Seismological Society of America 109, 1635–1652. https://doi.org/10.1785/0120190035
Hough, S.E., 2015. Shaking intensity from injection-induced versus tectonic earthquakes in the central-eastern United States. The Leading Edge 34, 690–697. https://doi.org/10.1190/tle34060690.1
Hough, S.E., 2014. Shaking from Injection-Induced Earthquakes in the Central and Eastern United States. Bulletin of the Seismological Society of America 104, 2619–2626. https://doi.org/10.1785/0120140099
Hough, S.E., 2001. Empirical Green's Function Analysis of Recent Moderate Events in California. Bulletin of the Seismological Society of America 91, 456–467. https://doi.org/10.1785/0119970154
Hough, S.E., 1997. Empirical Green's function analysis: Taking the next step. J. Geophys. Res. 102, 5369–5384. https://doi.org/10.1029/96JB03488
Huang, Y., Ellsworth, W.L., Beroza, G.C., 2017. Stress drops of induced and tectonic earthquakes in the central United States are indistinguishable. Science Advances 8.
Ide, S., 2001. Complex source processes and the interaction of moderate earthquakes during the earthquake swarm in the Hida-Mountains, Japan, 1998. Tectonophysics 334, 35–54. https://doi.org/10.1016/S0040-1951(01)00027-0
Ide, S., Beroza, G.C., 2001. Does apparent stress vary with earthquake size? Geophys. Res. Lett. 28, 3349–3352. https://doi.org/10.1029/2001GL013106

Igonin, N., Verdon, J.P., Kendall, J. - Michael, Eaton, D.W., 2021. Large- Scale Fracture Systems Are Permeable Pathways for Fault Activation During Hydraulic Fracturing. J Geophys Res Solid Earth 126. https://doi.org/10.1029/2020JB020311

Igonin, N., Zecevic, M., Eaton, D.W., 2018. Bilinear Magnitude- Frequency Distributions and Characteristic Earthquakes During Hydraulic Fracturing. Geophysical Research Letters 9.

Imanishi, K., Ellsworth, W.L., 2006. Source scaling relationships of microearthquakes at Parkfield, CA, determined using the SAFOD Pilot Hole Seismic Array, in: Abercrombie, R., McGarr, A., Kanamori, H., Di Toro, G. (Eds.), Geophysical Monograph Series. American Geophysical Union, Washington, D. C., pp. 81–90. https://doi.org/10.1029/170GM10

Jones, L.E., Helmberger, D.V., 1996. Seismicity and stress-drop in the Eastern Transverse Ranges, southern California. Geophys. Res. Lett. 23, 233–236. https://doi.org/10.1029/96GL00012

Kanamori, H., 2004. Static and Dynamic Scaling Relations for Earthquakes and Their Implications for Rupture Speed and Stress Drop. Bulletin of the Seismological Society of America 94, 314–319. https://doi.org/10.1785/0120030159

Kaneko, Y., Shearer, P.M., 2015. Variability of seismic source spectra, estimated stress drop, and radiated energy, derived from cohesive- zone models of symmetrical and asymmetrical circular and elliptical ruptures. J. Geophys. Res. Solid Earth 120, 1053–1079. https://doi.org/10.1002/2014JB011642

Kaneko, Y., Shearer, P.M., 2014. Seismic source spectra and estimated stress drop derived from cohesive-zone models of circular subshear rupture. Geophysical Journal International 197, 1002–1015. https://doi.org/10.1093/gji/ggu030

Klinger, A.G., Werner, M.J., 2021. Stress drops of hydraulic fracturing induced microseismicity in the Horn River basin: challenges at high frequencies recorded by borehole geophones. Geophysical Journal International 228, 2018–2037. https://doi.org/10.1093/gji/ggab458

Knapp, L.J., McMillan, J.M., Harris, N.B., 2017. A depositional model for organic-rich Duvernay Formation mudstones. Sedimentary Geology 347, 160–182. https://doi.org/10.1016/j.sedgeo.2016.11.012

Ktenidou, O.-J., Cotton, F., Abrahamson, N.A., Anderson, J.G., 2014. Taxonomy of : A Review of Definitions and Estimation Approaches Targeted to Applications. Seismological Research Letters 85, 135–146. https://doi.org/10.1785/0220130027

Lei, X., Su, J., Wang, Z., 2020. Growing seismicity in the Sichuan Basin and its association with industrial activities. Sci. China Earth Sci. 63, 1633–1660. https://doi.org/10.1007/s11430-020-9646-x

Madariaga, R., 1976. Dynamics of an expanding circular fault. Bulletin of the Seismological Society of America 66, 639–666. https://doi.org/10.1785/BSSA0660030639

McGuire, J.J., Kaneko, Y., 2018. Directly estimating earthquake rupture area using second moments to reduce the uncertainty in stress drop. Geophysical Journal International 214, 2224–2235. https://doi.org/10.1093/gji/ggy201

Mori, J., Frankel, A., 1990. Source parameters for small events associated with the 1986 North Palm Springs, California, earthquake determined using empirical Green functions. Bulletin of the Seismological Society of America 80, 278–295. https://doi.org/10.1785/BSSA0800020278

Negishi, H., Mori, J., Sato, T., Singh, R., Kumar, S., Hirata, N., 2002. Size and orientation of the fault plane for the 2001 Gujarat, India earthquake (Mw7.7) from aftershock observations: A high stress drop event. Geophys. Res. Lett. 29, 10-1-10–4. https://doi.org/10.1029/2002GL015280

Oth, A., Bindi, D., Parolai, S., Di Giacomo, D., 2011. Spectral Analysis of K-NET and KiK-net Data in Japan, Part II: On Attenuation Characteristics, Source Spectra, and Site Response of Borehole and Surface Stations. Bulletin of the Seismological Society of America 101, 667–687. https://doi.org/10.1785/0120100135

Oth, A., Bindi, D., Parolai, S., Di Giacomo, D., 2010. Earthquake scaling characteristics and the scale-(in)dependence of seismic energy-to-moment ratio: Insights from KiK-net data in Japan: EARTHQUAKE SCALING IN JAPAN. Geophys. Res. Lett. 37, n/a-n/a. https://doi.org/10.1029/2010GL044572

Oth, A., Kaiser, A.E., 2014. Stress Release and Source Scaling of the 2010–2011 Canterbury, New Zealand Earthquake Sequence from Spectral Inversion of Ground Motion Data. Pure Appl. Geophys. 171, 2767–2782. https://doi.org/10.1007/s00024-013-0751-1

Pacor, F., Spallarossa, D., Oth, A., Luzi, L., Puglia, R., Cantore, L., Mercuri, A., D'Amico, M., Bindi, D., 2016. Spectral models for ground motion prediction in the L'Aquila region (central Italy): evidence for stress-drop dependence on magnitude and depth. Geophys. J. Int. 204, 697–718. https://doi.org/10.1093/gji/ggv448

Paes, A. da S., 2020. Towards real-time microseismic processing: Efficient and robust methods for event detection and automated arrival time picking. University of Calgary, Calgary. Alberta, Canada.

Peacock, D.C.P., Nixon, C.W., Rotevatn, A., Sanderson, D.J., Zuluaga, L.F., 2016. Glossary of fault and other fracture networks. Journal of Structural Geology 92, 12–29. https://doi.org/10.1016/j.jsg.2016.09.008

Pedregosa, F., Varoquaux, G., Gramfort, A., Michel, V., Thirion, B., Grisel, O., Blondel, M., Prettenhofer, P., Weiss, R., Dubourg, V., Vanderplas, J., 2011. Scikit-learn: Machine learning in Python. The Journal of Machine Learning Research 12, 2825–2830.

Pennington, C.N., Chen, X., Abercrombie, R.E., Wu, Q., 2021. Cross Validation of Stress Drop Estimates and Interpretations for the 2011 Prague, OK, Earthquake Sequence Using Multiple Methods. J Geophys Res Solid Earth 126. https://doi.org/10.1029/2020JB020888

Pennington, C.N., Uchide, T., Chen, X., 2022. Slip Characteristics of Induced Earthquakes: Insights From the 2015 M_w 4.0 Guthrie, Oklahoma Earthquake. JGR Solid Earth 127. https://doi.org/10.1029/2021JB023564

Pollard, D.D., Aydin, A., 1988. Progress in understanding jointing over the past century. Geological Society of America Bulletin 100, 1181–1204. https://doi.org/10.1130/0016-7606(1988)100<1181:PIUJOT>2.3.CO;2

Poulin, A., Weir, R., Eaton, D., Igonin, N., Chen, Y., Lines, L., Lawton, D., 2019. Focal-time analysis: A new method for stratigraphic depth control of microseismicity and induced seismic events. Geophysics 84, 10. https://doi.org/10.1190/GEO2019-0046.1

Prieto, G.A., 2022. The *Multitaper* Spectrum Analysis Package in Python. Seismological Research Letters 93, 1922–1929. https://doi.org/10.1785/0220210332

Reiter, D., Leidig, M., Yoo, S.-H., Mayeda, K., 2012. Source characteristics of seismicity associated with underground wastewater disposal: A case study from the 2008 Dallas-Fort Worth earthquake sequence. The Leading Edge 31, 1454–1460. https://doi.org/10.1190/tle31121454.1

Rodríguez-Pradilla, G., Eaton, D.W., 2019. The Application of Coda and Energy Methods for Magnitude Estimation of Microseismic Events. Seismological Research Letters 90, 12. https://doi.org/10.1785/0220180366

Rubin, A.M., Ampuero, J.-P., 2005. Earthquake nucleation on (aging) rate and state faults: RATE AND STATE EARTHQUAKE NUCLEATION. J. Geophys. Res. 110. https://doi.org/10.1029/2005JB003686

Ruhl, C.J., Abercrombie, R.E., Smith, K.D., 2017. Spatiotemporal Variation of Stress Drop During the 2008 Mogul, Nevada, Earthquake Swarm: Stress Drops of the 2008 Mogul, NV, Swarm. J. Geophys. Res. Solid Earth 122, 8163–8180. https://doi.org/10.1002/2017JB014601

Schultz, R., Skoumal, R.J., Brudzinski, M.R., Eaton, D., Baptie, B., Ellsworth, W., 2020. Hydraulic Fracturing- Induced Seismicity. Reviews of Geophysics 43.

Shearer, P.M., Abercrombie, R.E., 2021. Calibrating Spectral Decomposition of Local Earthquakes Using Borehole Seismic Records—Results for the 1992 Big Bear Aftershocks in Southern California. J Geophys Res Solid Earth 126. https://doi.org/10.1029/2020JB020561

Shearer, P.M., Abercrombie, R.E., Trugman, D.T., Wang, W., 2019. Comparing EGF Methods for Estimating Corner Frequency and Stress Drop From *P* Wave Spectra. J. Geophys. Res. Solid Earth 124, 3966–3986. https://doi.org/10.1029/2018JB016957

Shearer, P.M., Prieto, G.A., Hauksson, E., 2006. Comprehensive analysis of earthquake source spectra in southern California: SOUTHERN CALIFORNIA SOURCE SPECTRA. J. Geophys. Res. 111, n/a-n/a. https://doi.org/10.1029/2005JB003979

Spottiswoode, S., McGarr, A., 1975. Source parameters of tremors in a deep-level gold mine. Bulletin of the Seismological Society of America 65. https://doi.org/10.1785/BSSA0650010093

Sumy, D.F., Neighbors, C.J., Cochran, E.S., Keranen, K.M., 2017. Low stress drops observed for aftershocks of the 2011 M_w 5.7 Prague, Oklahoma, earthquake. J. Geophys. Res. Solid Earth 122, 3813–3834. https://doi.org/10.1002/2016JB013153

Tomic, J., Abercrombie, R.E., do Nascimento, A.F., 2009. Source parameters and rupture velocity of small $M \leq 2.1$ reservoir induced earthquakes. Geophysical Journal International 179, 1013–1023. https://doi.org/10.1111/j.1365-246X.2009.04233.x

Trugman, D.T., 2022. Resolving Differences in the Rupture Properties of M5 Earthquakes in California Using Bayesian Source Spectral Analysis. JGR Solid Earth 127. https://doi.org/10.1029/2021JB023526

Trugman, D.T., 2020. Stress-Drop and Source Scaling of the 2019 Ridgecrest, California, Earthquake Sequence. Bulletin of the Seismological Society of America 110, 1859–1871. https://doi.org/10.1785/0120200009

Trugman, D.T., Dougherty, S.L., Cochran, E.S., Shearer, P.M., 2017. Source Spectral Properties of Small to Moderate Earthquakes in Southern Kansas. J. Geophys. Res. Solid Earth 122, 8021–8034. https://doi.org/10.1002/2017JB014649

Trugman, D.T., Ross, Z.E., Johnson, P.A., 2020. Imaging Stress and Faulting Complexity Through Earthquake Waveform Similarity. Geophysical Research Letters 8.

Trugman, D.T., Shearer, P.M., 2018. Strong Correlation between Stress Drop and Peak Ground Acceleration for Recent M 1–4 Earthquakes in the San Francisco Bay Area. Bulletin of the Seismological Society of America 108, 929–945. https://doi.org/10.1785/0120170245

Trugman, D.T., Shearer, P.M., 2017. Application of an improved spectral decomposition method to examine earthquake source scaling in Southern California. J. Geophys. Res. Solid Earth 122, 2890–2910. https://doi.org/10.1002/2017JB013971

Tullis, T.E., 2015. Mechanisms for Friction of Rock at Earthquake Slip Rates, in: Treatise on Geophysics. Elsevier, pp. 139–159. https://doi.org/10.1016/B978-0-444-53802-4.00073-7

Uchida, N., Shimamura, K., Matsuzawa, T., Okada, T., 2015. Postseismic response of repeating earthquakes around the 2011 Tohoku-oki earthquake: Moment increases due to the fast loading rate. J. Geophys. Res. Solid Earth 120, 259–274. https://doi.org/10.1002/2013JB010933

Uchide, T., Imanishi, K., 2016. Small Earthquakes Deviate from the Omega‐ Square Model as Revealed by Multiple Spectral Ratio Analysis. Bulletin of the Seismological Society of America 106, 1357–1363. https://doi.org/10.1785/0120150322

Venkataraman, A., Kanamori, H., 2004. Observational constraints on the fracture energy of subduction zone earthquakes. J. Geophys. Res. 109. https://doi.org/10.1029/2003JB002549

Viegas, G., Abercrombie, R.E., Kim, W.-Y., 2010. The 2002 M5 Au Sable Forks, NY, earthquake sequence: Source scaling relationships and energy budget. J. Geophys. Res. 115, B07310. https://doi.org/10.1029/2009JB006799

Viegas, G., Baig, A., Coulter, W., Urbancic, T., 2012. Effective monitoring of reservoir-induced seismicity utilizing integrated surface and downhole seismic networks. First Break 30. https://doi.org/10.3997/1365-2397.30.7.60347

von Luxburg, U., 2007. A tutorial on spectral clustering. Stat Comput 17, 395–416. https://doi.org/10.1007/s11222-007-9033-z

Walter, W.R., Mayeda, K., Gok, R., Hofstetter, A., 2006. The scaling of seismic energy with moment: Simple models compared with observations, in: Abercrombie, R., McGarr, A., Kanamori, H., Di Toro, G. (Eds.), Geophysical Monograph Series. American Geophysical Union, Washington, D. C., pp. 25–41. https://doi.org/10.1029/170GM05

Walter, W.R., Yoo, S., Mayeda, K., Gök, R., 2017. Earthquake stress via event ratio levels: Application to the 2011 and 2016 Oklahoma seismic sequences. Geophys. Res. Lett. 44, 3147–3155. https://doi.org/10.1002/2016GL072348

Wang, E., Rubin, A.M., Ampuero, J.-P., 2014. Compound earthquakes on a bimaterial interface and implications for rupture mechanics. Geophysical Journal International 197, 1138–1153. https://doi.org/10.1093/gji/ggu047

Wang, H., Ren, Y., Wen, R., Xu, P., 2019. Breakdown of Earthquake Self‐ Similar Scaling and Source Rupture Directivity in the 2016–2017 Central Italy Seismic Sequence. J. Geophys. Res. Solid Earth 124, 3898–3917. https://doi.org/10.1029/2018JB016543

Wang, R., Weingarten, M., Langenbruch, C., DeShon, H.R., 2020. Introduction to the Special Section on Observations, Mechanisms, and Hazards of Induced Seismicity 6.

Weir, R.M., Eaton, D.W., Lines, L.R., Lawton, D.C., Ekpo, E., 2018. Inversion and interpretation of seismic-derived rock properties in the Duvernay play. Interpretation 6, SE1–SE14. https://doi.org/10.1190/INT-2017-0149.1

Wen, J., Chen, X., Xu, J., 2018. A Dynamic Explanation for the Ruptures of Repeating Earthquakes on the San Andreas Fault at Parkfield. Geophysical Research Letters 45. https://doi.org/10.1029/2018GL079140

Wu, Q., Chen, X., Abercrombie, R.E., 2019. Source Complexity of the 2015 Mw 4.0 Guthrie, Oklahoma Earthquake. Geophys. Res. Lett. 46, 4674–4684. https://doi.org/10.1029/2019GL082690

Yamada, T., 2005. Radiation efficiency and apparent stress of small earthquakes in a South African gold mine. J. Geophys. Res. 110, B01305. https://doi.org/10.1029/2004JB003221

Ye, L., Lay, T., Kanamori, H., Rivera, L., 2016. Rupture characteristics of major and great ($M_w \geq 7.0$) megathrust earthquakes from 1990 to 2015: 2. Depth dependence. J. Geophys. Res. Solid Earth 121, 845–863. https://doi.org/10.1002/2015JB012427

Yenier*, E., Laporte, M., Baturan, D., 2016. Induced-seismicity monitoring: Broadband seismometers and geophone comparison. Presented at the 2016 SEG International Exposition and Annual Meeting, p. SEG-2016-13970947.

Yin, J., Denolle, M.A., Yao, H., 2018. Spatial and Temporal Evolution of Earthquake Dynamics: Case Study of the M_w 8.3 Illapel Earthquake, Chile: 2015 Illapel earthquake source analysis. J. Geophys. Res. Solid Earth 123, 344–367. https://doi.org/10.1002/2017JB014265

Yu, H., Harrington, R.M., Kao, H., Liu, Y., Abercrombie, R.E., Wang, B., 2020. Well Proximity Governing Stress Drop Variation and Seismic Attenuation Associated With Hydraulic Fracturing Induced Earthquakes. J. Geophys. Res. Solid Earth 125. https://doi.org/10.1029/2020JB020103

Zhang, H., Eaton, D.W., Rodriguez, G., Jia, S.Q., 2019. Source-Mechanism Analysis and Stress Inversion for Hydraulic- Fracturing-Induced Event Sequences near Fox Creek, Alberta 16.

Mailing Addresses

Nadine Igonin
Bureau of Economic Geology
The University of Texas at Austin
P.O. Box X
Austin, TX 78713-8924

Daniel Trugman
Laxalt Mineral Engineering
Building, Room 322 (MS 0174)
University of Nevada, Reno
Reno, NV 89557

Keyla Gonzalez
TGS
10451 Clay Road
Houston, Texas
77041, USA

David Eaton
Earth Sciences 118
University of Calgary
2500 University Drive NW
Calgary, AB, Canada
T2N 1N4

LIST OF FIGURE CAPTIONS

Figure 1: a) Map view of ToC2ME seismicity epicenters scaled by magnitude, with events color-coded in time. Well trajectories are shown in white and the stations are indicated with green triangles. b) Distribution of the complete set of geophone arrays around the wells. The labels NS1, NS2, NESW, and NS3 denote different clusters of events, as described in the text.

Figure 2: Source spectra from an event on November 25, 00:03:43. a) Individual station spectra, colored by distance from the event. Black solid line shows the median. Noise spectra are shown in grey, and the white solid line is the median. The minimum and maximum frequency for the fit are shown as vertical dashed lines, and the inverted corner frequency is shown with the vertical white line. b) Bootstrap realizations of the median source spectra, colored by the best-fitting corner frequency. The Boatwright model is also plotted in blue with the median bootstrap corner frequency, and the background shading corresponds to 95% of the range of obtained fc values.

Figure 3: Cross plot of corner frequency and magnitude, with a line of best fit from the median of data binned at magnitude increments of 0.2 in the $\log_{10}(M_0)$ domain (black squares). Dark green symbols denote events for which the standard deviation of the inverted corner frequency was greater than 10 Hz. The two lighter shades of green are events with a standard deviation of less than 10 Hz, but the lighter circles have corner frequencies that are less than the SNR 2 threshold for the upper frequency limit (fmax in Figure 2a). Dashed lines of equal stress drop are labelled between 0.01 MPa and 100 MPa.

Figure 4: Normalized magnitude-corrected f_c. Time series for NS1(a) and NS3 (b). Occurrence of nearest hydraulic fracturing operations is shown with vertical lines colored by well; yellow for well A, red for well C and grey for well D. Thick black lines show the cumulative normalized fc. Circles are used for events along NS1 and squares are used for events along NS3. c) map view of NS1, with wells labelled and closest stages shown with 'x' symbols. d) map view of NS3.

Figure 5: Normalized magnitude-corrected f_c for the NE/SW trending features. a) Time series for with timing of nearest hydraulic fracturing operations shown with vertical lines colored by well; yellow for well A, white for well B, red for well C and grey for well D. Thick black line shows the cumulative normalized fc. b) Map view of NE/SW features. The magnitude 3.1 event is indicated on both panels and corresponds to an increase in normalized f_c for the cluster.

Figure 6: Normalized residual spectra by cluster, highlighting prevalence of high/low relative frequencies for certain clusters. Each subpanel (a-h) shows a different cluster, with the median of the cluster shown with a thick black line and one standard deviation shown with the thin black lines.

Figure 7: Spatial and temporal view by cluster from spectral clustering algorithm. Time series of events within a) NS1, b) NS3, and c) NESW. d) Map view of events colored by cluster from spectral clustering algorithm (Figure 6).

Figure 8: Histogram of normalized corner frequency depending on whether the event occurred on a fault (yellow) or a fracture network (magenta). The peaks of the two distributions are distinct, as illustrated by the solid lines (kernel density estimates).

All figures in a PDF with captions
Click here to access/download;Manuscript;FiguresOnly.pdf

FIGURES

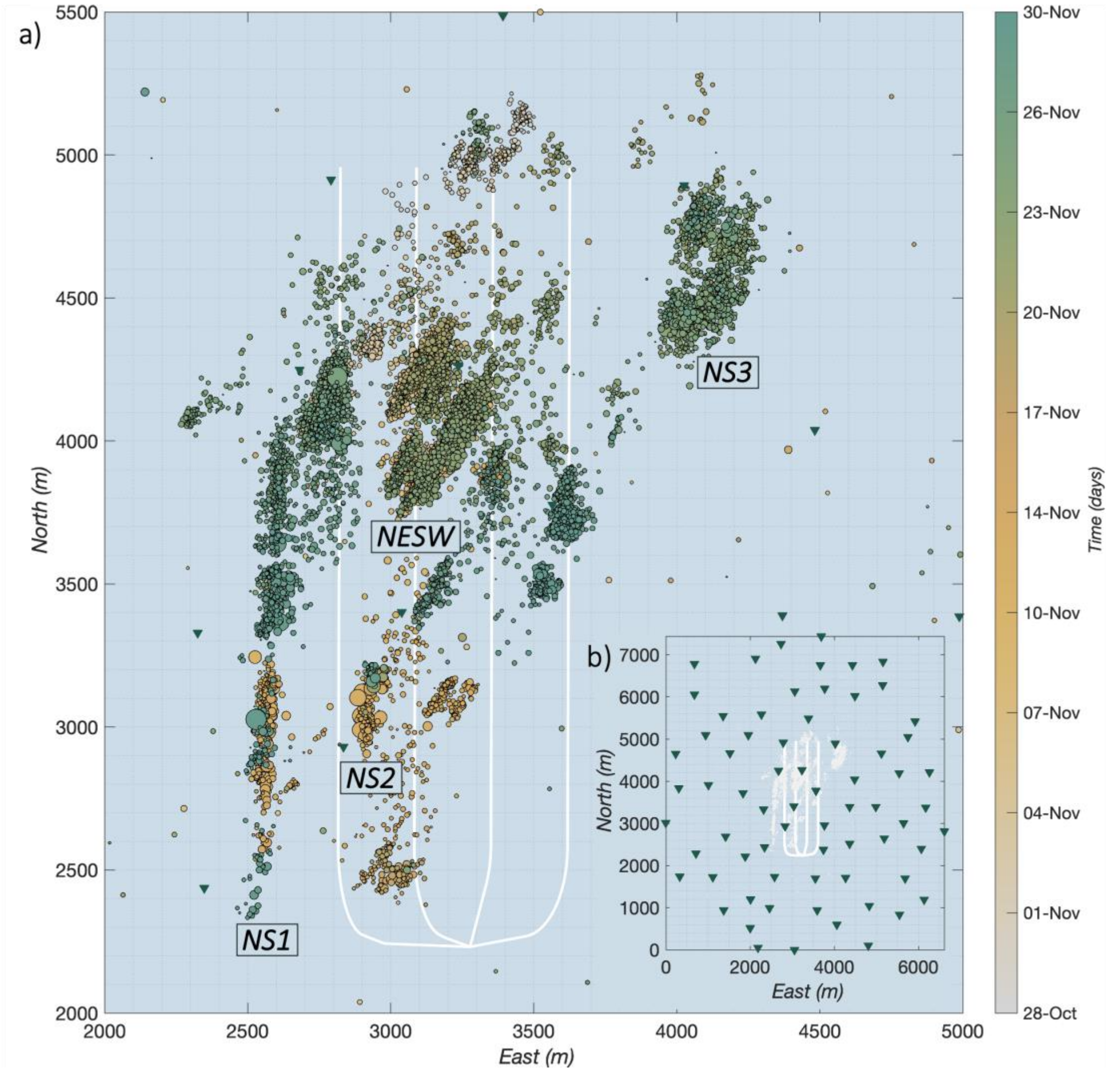

Figure 1: a) Map view of ToC2ME seismicity epicenters scaled by magnitude, with events color-coded in time. Well trajectories are shown in white and the stations are indicated with green triangles. b) Distribution of the complete set of geophone arrays around the wells. The labels NS1, NS2, NESW, and NS3 denote different clusters of events, as described in the text.

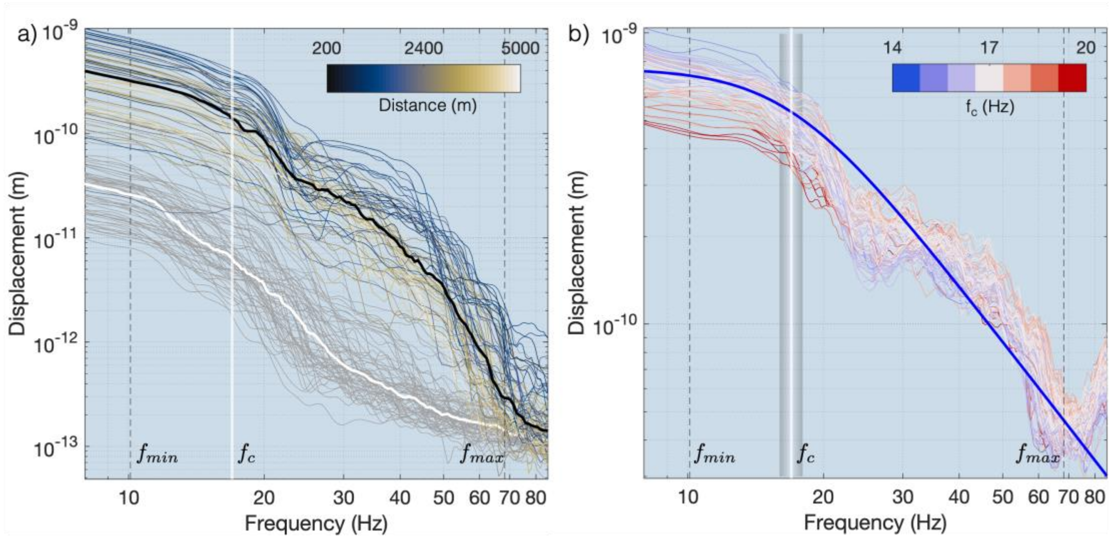

Figure 2: Source spectra from an event on November 25, 00:03:43. a) Individual station spectra, colored by distance from the event. Black solid line shows the median. Noise spectra are shown in grey, and the white solid line is the median. The minimum and maximum frequency for the fit are shown as vertical dashed lines, and the inverted corner frequency is shown with the vertical white line. b) Bootstrap realizations of the median source spectra, colored by the best-fitting corner frequency. The Boatwright model is also plotted in blue with the median bootstrap corner frequency, and the background shading corresponds to 95% of the range of obtained fc values.

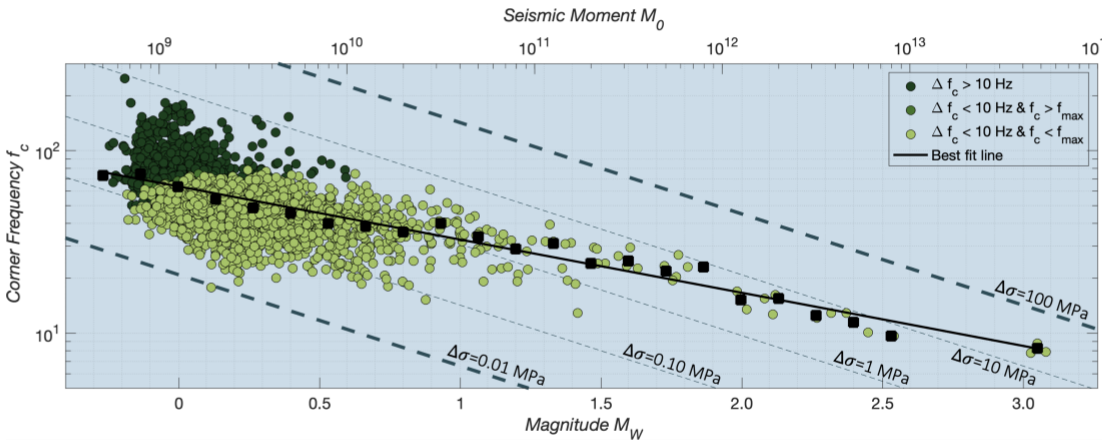

Figure 3: Cross plot of corner frequency and magnitude, with a line of best fit from the median of data binned at magnitude increments of 0.2 in the $log_{10}(M_0)$ domain (black squares). Dark green symbols denote events for which the standard deviation of the inverted corner frequency was greater than 10 Hz. The two lighter shades of green are events with a standard deviation of less than 10 Hz, but the lighter circles have corner frequencies that are less than the SNR 2 threshold for the upper frequency limit (fmax in Figure 2a). Dashed lines of equal stress drop are labelled between 0.01 MPa and 100 MPa.

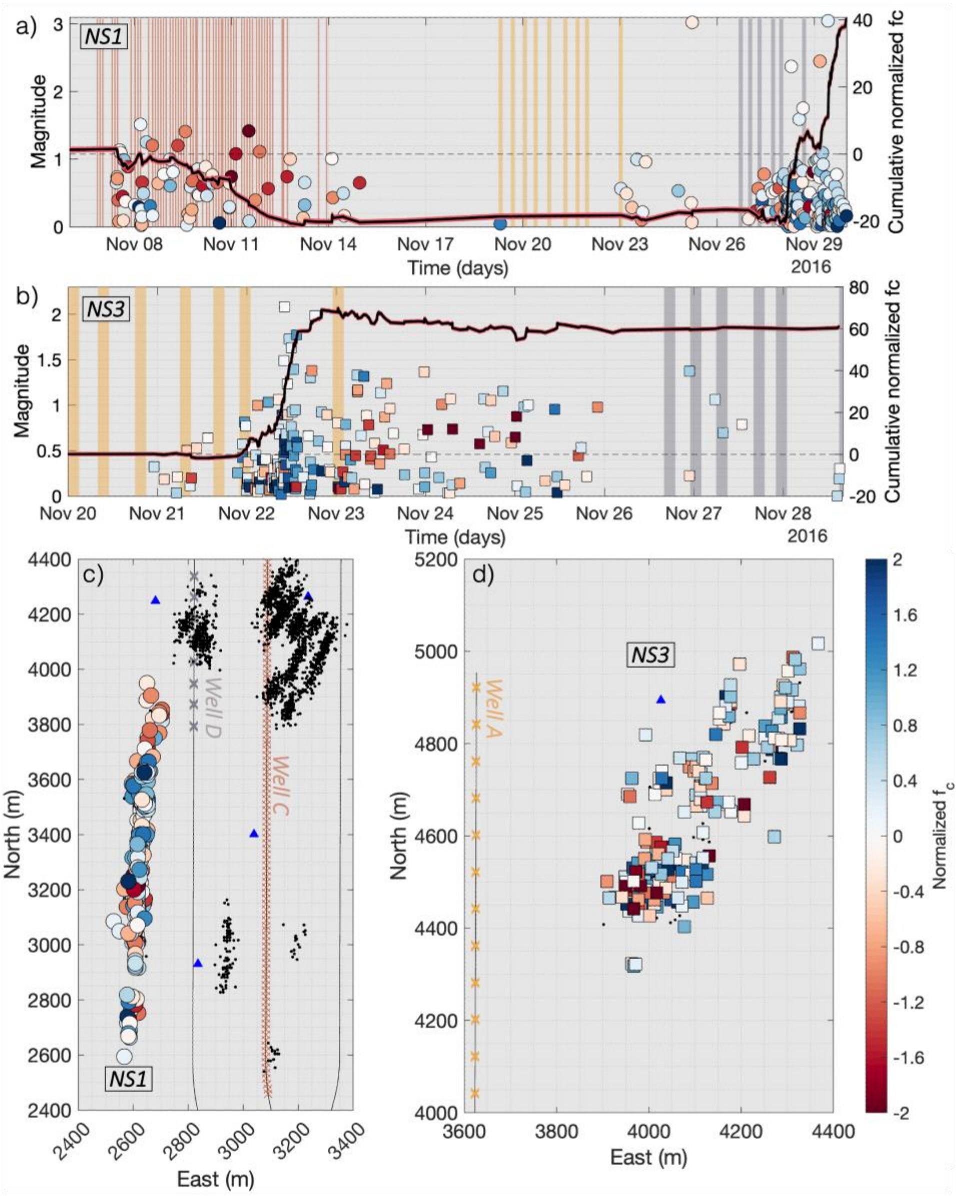

Figure 4: Normalized magnitude-corrected f_c. Time series for NS1(a) and NS3 (b). Occurrence of nearest hydraulic fracturing operations is shown with vertical lines colored by well; yellow for well A, red for well C and grey for well D. Thick black lines show the cumulative normalized fc. Circles are used for events along NS1 and squares are used for events along NS3. c) map view of NS1, with wells labelled and closest stages shown with 'x' symbols. d) map view of NS3.

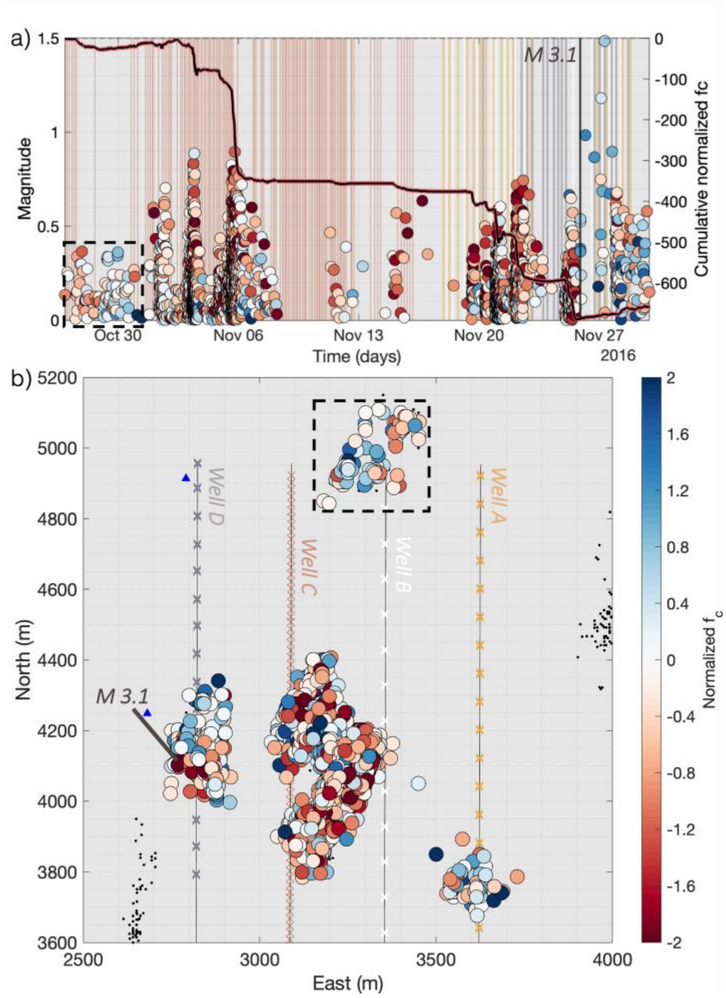

Figure 5: Normalized magnitude-corrected f_c for the NE/SW trending features. a) Time series for with timing of nearest hydraulic fracturing operations shown with vertical lines colored by well; yellow for well A, white for well B, red for well C and grey for well D. Thick black line shows the cumulative normalized fc. b) Map view of NE/SW features. The magnitude 3.1 event is indicated on both panels and corresponds to an increase in normalized f_c for the cluster.

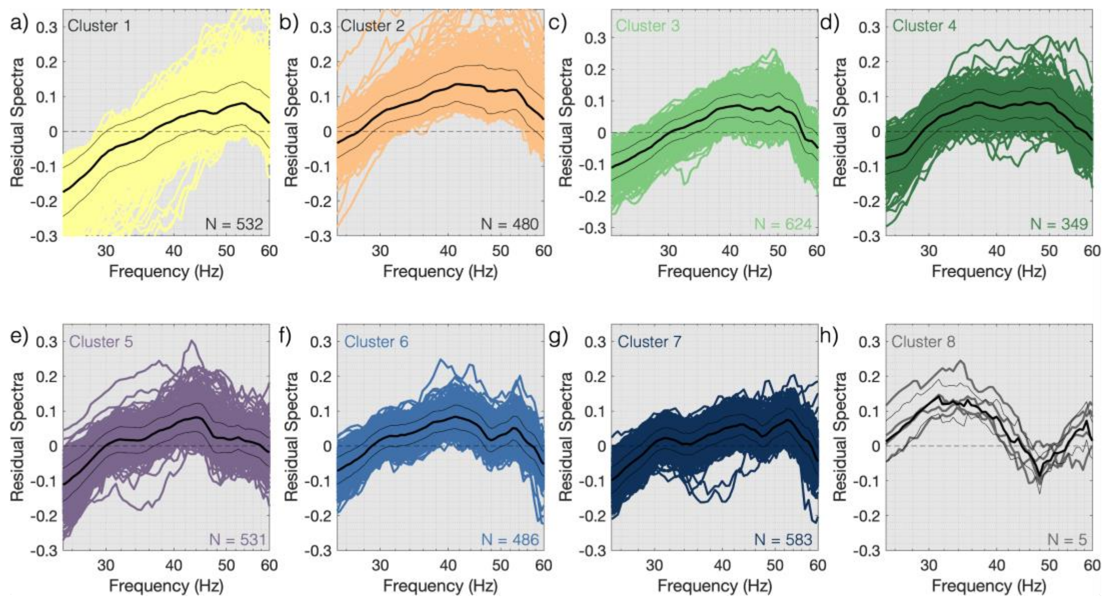

Figure 6: Normalized residual spectra by cluster, highlighting prevalence of high/low relative frequencies for certain clusters. Each subpanel (a-h) shows a different cluster, with the median of the cluster shown with a thick black line and one standard deviation shown with the thin black lines.

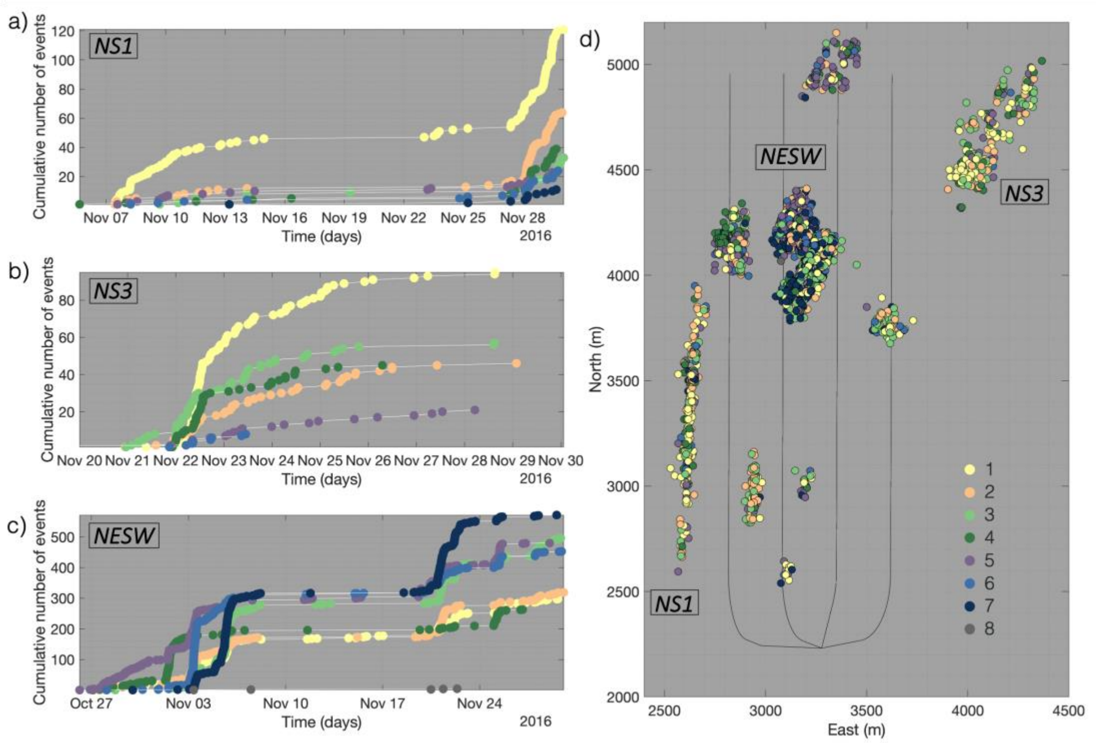

Figure 7: Spatial and temporal view by cluster from spectral clustering algorithm. Time series of events within a) NS1, b) NS3, and c) NESW. d) Map view of events colored by cluster from spectral clustering algorithm (Figure 6).

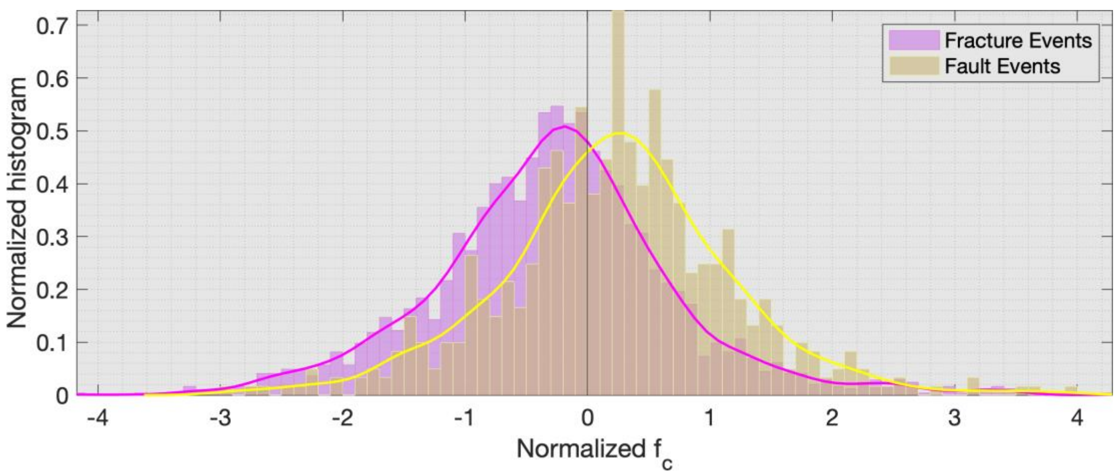

Figure 8: Histogram of normalized corner frequency depending on whether the event occurred on a fault (yellow) or a fracture network (magenta). The peaks of the two distributions are distinct, as illustrated by the solid lines (kernel density estimates).